Phase-Sensitive Coherence and the Classical-Quantum Boundary in Ghost Imaging

Baris I. Erkmen[a], Nicholas D. Hardy[b], Dheera Venkatraman[b], Franco N. C. Wong[b], and Jeffrey H. Shapiro[b]

[a]Jet Propulsion Laboratory, California Institute of Technology, 4800 Oak Grove Drive, Pasadena CA 91109, USA.

[b]Research Laboratory of Electronics, Massachusetts Institute of Technology, 77 Massachusetts Avenue, Cambridge, MA 02139, USA.

ABSTRACT

The theory of partial coherence has a long and storied history in classical statistical optics. The vast majority of this work addresses fields that are statistically stationary in time, hence their complex envelopes only have phase-insensitive correlations. The quantum optics of squeezed-state generation, however, depends on nonlinear interactions producing baseband field operators with phase-insensitive and phase-sensitive correlations. Utilizing quantum light to enhance imaging has been a topic of considerable current interest, much of it involving biphotons, i.e., streams of entangled-photon pairs. Biphotons have been employed for quantum versions of optical coherence tomography, ghost imaging, holography, and lithography. However, their seemingly quantum features have been mimicked with classical-state light, questioning wherein lies the classical-quantum boundary. We have shown, for the case of Gaussian-state light, that this boundary is intimately connected to the theory of phase-sensitive partial coherence. Here we present that theory, contrasting it with the familiar case of phase-insensitive partial coherence, and use it to elucidate the classical-quantum boundary of ghost imaging. We show, both theoretically and experimentally, that classical phase-sensitive light produces ghost images most closely mimicking those obtained with biphotons, and we derive the spatial resolution, image contrast, and signal-to-noise ratio of a standoff-sensing ghost imager, taking into account target-induced speckle.

Keywords: optical imaging, quantum imaging, coherence theory, ghost imaging, phase-sensitive coherence

1. INTRODUCTION

Central to modern-optics theory is the concept of optical coherence. Optical fields that have finite spatial extent and finite radiation bandwidth around a center frequency are superpositions of monochromatic plane waves. The degree of correlation between these plane-wave components defines the field's spatial and temporal coherence properties. As an example, consider a paraxially-propagating optical field. Its transverse coherence length is the minimum spatial separation between two observation points on a transverse plane that yields uncorrelated fluctuations. A spatially coherent beam is one whose transverse coherence length equals its cross-section diameter. At the opposite extreme, we have a spatially incoherent beam, whose transverse coherence length is only a fraction of the center wavelength. Similar classifications exist for the other dimensions of an optical field as well, such as its coherence in time and polarization. Often times, however, optical fields generated by real-world sources do not exhibit the two extremes of perfect coherence or incoherence, but rather have an intermediate degree of coherence. These fields are said to be partially coherent, and the study of their statistical properties constitutes the theory of *partial coherence*.

Although a detailed account of the history of partial-coherence theory is beyond the scope of this paper, we would be remiss to not recount some of the pioneering efforts in this field. The earliest observation and characterization efforts for spatial and temporal coherence date to the mid-19th century.[1] However, Van Cittert and independently Zernike are credited with the earliest quantitative treatments of correlations between optical fields observed at two observation points separated either in space or time.[1] The well-known Van Cittert-Zernike

Send correspondence to B.I.E. at baris.i.erkmen@jpl.nasa.gov.

theorem—which we make use of in this paper—for the propagation of partial coherence through free space is named in reference to these pioneering early results. Nonetheless, it is not an exaggeration to say that the rigorous theory of partial coherence is founded in large part by seminal researchers such as M. Born, E. Wolf, L. Mandel, and J. W. Goodman.[1–3] Statistical optics, which is a classical theory of light that models the fluctuations in optical fields as random and studies their—second-order and higher—moments, is utilized across virtually all optics disciplines, including optical imaging, spectroscopy, metrology, remote-sensing, and ranging etc.[3,4]

In this paper we will limit our scope to the complex baseband envelope of a quasimonochromatic and paraxially-propagating partially-coherent field. The complex baseband envelope has two types of second-order correlation functions, referred to as the phase-insensitive correlation function and the phase-sensitive correlation function.[5] In order to fully describe the second-order coherence behavior of the optical field, *both* of these correlations must be specified. Yet, traditional optical coherence theory—for both classical and quantum fields—has been developed almost exclusively for the phase-insensitive correlation function. This is because commonly encountered sources (e.g, sunlight, light-emitting diodes, lasers) do not have phase-sensitive correlations.[2,3] However, with advances in nonlinear and quantum optics, we are presently able to generate optical fields that have nonzero phase-sensitive correlations. The best known example for such fields are the squeezed states of light.[6] In addition, the biphoton state,[7] which has received a great deal of recent attention owing to its entanglement properties, is the low-brightness and low-flux limit of the signal and idler fields generated by spontaneous parametric downconversion.[8] Each of these fields possesses a nonzero phase-insensitive autocorrelation, but, more importantly, they have a phase-sensitive cross correlation that is *stronger* than that permitted by classical statistical optics. Note that classical fields can also have non-zero phase-sensitive correlation. Thus, understanding phase-sensitive coherence and its properties is central to developing a unified view of second-order coherence for classical and quantum fields. Here we will build on our earlier development of this theory,[9] and study the paraxial propagation of phase-sensitive coherence, contrasting it to that of the well-known propagation behavior of phase-insensitive coherence.

The phase-sensitive coherence theory we present here will then be utilized in studying ghost imaging, a transverse imaging modality that has been receiving considerable and increasing attention of late owing to its novel physical characteristics and its potential applications to remote sensing. Ghost imaging exploits the cross correlation between the photocurrents obtained from illumination of two spatially-separated photodetectors by a pair of highly-correlated, partially-coherent optical beams. One beam interrogates a target (or sample) and then illuminates a single-pixel (bucket) detector that provides no spatial resolution. The other beam does not interact with the target, but it impinges on a scanning pinhole detector or a high-resolution camera, hence affording a multi-pixel output. The term "ghost imaging" refers to the fact that neither photocurrent alone yields a target image, but cross-correlating the two photocurrents does produce an image.

Although phase-sensitive coherence has thus far been demonstrated in nonclassical sources (e.g., squeezed states and the biphoton state), classical beams too can possess this correlation. The final section of our paper is devoted to presenting a recent experimental demonstration of ghost imaging using *classical* phase-sensitive Gaussian-state light. This experiment validates the key predictions of phase-sensitive coherence theory in ghost imaging: (1) that Gaussian-state sources with phase-sensitive coherence yield an inverted ghost image in the far field; and (2) that its spatial resolution equals that of the ghost image formed using a phase-insensitive Gaussian-state source whose autocorrelation function matches that of the phase-sensitive source. This experiment also identifies some practical issues with utilizing phase-sensitive coherence that were not included in our theoretical treatment.

Throughout this paper we shall use quantum-mechanical notation. It is important to keep in mind, however, that when the quantum field operators are in coherent states or statistical mixtures thereof, the quantitative predictions derived using this theory coincide precisely with those derived using classical statistical optics and the semiclassical—shot-noise—theory of photodetection.[5,10] Therefore, we refer to observations that have a quantitative explanation using the latter theory as *classical* outcomes. If, on the other hand, the observation can *only* be explained with the quantum theory of light, we refer to it as a *quantum* or *nonclassical* outcome.

Our paper is organized as follows. In Section 2 we begin with the fundamentals of quasimonochromatic, paraxial propagation of optical beams having phase-sensitive and phase-insensitive partial coherence. We utilize Gaussian-Schell model second-order correlation functions to delineate the differences between the free-space

propagation of these two types of coherence. In Section 3, we then apply this theory to study ghost imaging in a standoff-sensing scenario, emphasizing the role of target-induced speckle. In Section 4 we present a ghost imaging experiment using classical phase-sensitive light, obtained by imposing complex-conjugate modulations in the signal- and reference-arm beams of ghost imaging. In Section 5, we conclude by revisiting some of the key points that we have made.

2. PHASE-SENSITIVE COHERENCE THEORY

Let $\hat{E}_z(\boldsymbol{\rho},t)e^{-i\omega_0 t}$ denote a $+z$-propagating, scalar, positive-frequency, electric-field operator with center frequency ω_0, where $\boldsymbol{\rho}$ denotes the transverse spatial coordinate on the z plane, and t denotes time. Here, $\hat{E}_z$ is the $\sqrt{\text{photons/m}^2\text{s}}$-units baseband field operator with commutators $[\hat{E}_z(\boldsymbol{\rho}_1,t_1),\hat{E}_z^\dagger(\boldsymbol{\rho}_2,t_2)]=\delta(\boldsymbol{\rho}_1-\boldsymbol{\rho}_2)\delta(t_1-t_2)$ and $[\hat{E}_z(\boldsymbol{\rho}_1,t_1),\hat{E}_z(\boldsymbol{\rho}_2,t_2)]=0$. Throughout this paper we shall assume that $\hat{E}_z(\boldsymbol{\rho},t)$ is is in a zero-mean Gaussian state, such that it is fully specified by its phase-insensitive and phase-sensitive autocorrelation functions, $\langle\hat{E}_z^\dagger(\boldsymbol{\rho}_1,t_1)\hat{E}_z(\boldsymbol{\rho}_2,t_2)\rangle$ and $\langle\hat{E}_z(\boldsymbol{\rho}_1,t_1)\hat{E}_z(\boldsymbol{\rho}_2,t_2)\rangle$ respectively. Note that a nonzero phase-sensitive correlation function implies that the Hermitian passband field operator $\hat{\mathcal{E}}(\boldsymbol{\rho},t)=\hat{E}_z(\boldsymbol{\rho},t)e^{-i\omega_0 t}+\hat{E}_z^\dagger(\boldsymbol{\rho},t)e^{i\omega_0 t}$, associated with $\hat{E}_z(\boldsymbol{\rho},t)$, has a nonstationary phase-sensitive correlation function.* Because most natural-occurring optical fields are stationary, they do not exhibit phase-sensitive coherence. However, a broad class of nonstationary optical fields has been generated. The prototypical example of phase-sensitive light is the squeezed state, whose passband, $\hat{\mathcal{E}}$, properties are nonstationary even when its complex-envelope, $\hat{E}_z$, behavior is stationary.[5]

In order to highlight the distinctions between phase-insensitive and phase-sensitive coherence, we shall adopt the simplification that the correlation functions are cross-spectrally pure and have Gaussian-Schell form.[2,3] First, let the phase-insensitive correlation function be given by

$$\langle\hat{E}^\dagger(\boldsymbol{\rho}_1,t_1)\hat{E}(\boldsymbol{\rho}_2,t_2)\rangle=\frac{2P}{\pi a_0^2}e^{-(|\boldsymbol{\rho}_1|^2+|\boldsymbol{\rho}_2|^2)/a_0^2-|\boldsymbol{\rho}_2-\boldsymbol{\rho}_1|^2/2\rho_0^2}e^{-(t_2-t_1)^2/2T_0^2}, \tag{1}$$

where P denotes the mean photon flux, a_0 is the beam radius defined as the radius at which the photon irradiance profile is attenuated by e^{-2} relative to the peak beam irradiance, ρ_0 is the coherence radius, and T_0 is the coherence time. We assume that the field has low spatial coherence, i.e., $\rho_0 \ll a_0$. So, the phase-insensitive fluctuations observed at the space-time coordinates $(\boldsymbol{\rho}_1,t_1)$ and $(\boldsymbol{\rho}_2,t_2)$ are correlated when $\boldsymbol{\rho}_1$ and $\boldsymbol{\rho}_2$ are separated by a distance smaller than the coherence length ρ_0, while both are within the beam radius a_0, and when t_1 and t_2 are separated by less than the coherence time T_0. If we write the baseband field operator in terms of its monochromatic plane-wave components,

$$\hat{E}(\boldsymbol{\rho},t)=\int_{\mathbb{R}^2}\frac{\mathrm{d}\boldsymbol{k}}{2\pi}\int_{-\infty}^{\infty}\frac{\mathrm{d}\Omega}{\sqrt{2\pi}}\hat{A}(\boldsymbol{k},\Omega)e^{i\boldsymbol{k}\cdot\boldsymbol{\rho}-i\Omega t}. \tag{2}$$

where $\boldsymbol{k}$ is transverse spatial-frequency vector and Ω is the temporal frequency, we obtain

$$\langle\hat{A}^\dagger(\boldsymbol{k}_1,\Omega_1)\hat{A}(\boldsymbol{k}_2,\Omega_2)\rangle=\frac{PT_0\rho_0^2}{\sqrt{2\pi}}e^{-a_0^2|\boldsymbol{k}_d|^2/8-\rho_0^2|\boldsymbol{k}_s|^2/2}e^{-T_0^2\Omega_2^2/2}\delta(\Omega_2-\Omega_1)\,, \tag{3}$$

where $\boldsymbol{k}_s\equiv(\boldsymbol{k}_1+\boldsymbol{k}_2)/2$ and $\boldsymbol{k}_d\equiv\boldsymbol{k}_2-\boldsymbol{k}_1$, and we have used the low-coherence condition to write $1/a_0^2+1/\rho_0^2\approx 1/\rho_0^2$. As shown in Fig. 1(a), this correlation function implies that the angular extent of the source radiation (found by setting $\boldsymbol{k}_d=\boldsymbol{0}$) is $2\lambda_0/\pi\rho_0$, and that the angular extent of the source coherence (found by setting $\boldsymbol{k}_s=\boldsymbol{0}$), is $2\lambda_0/\pi a_0$, where $\lambda_0\equiv 2\pi c/\omega_0$ is the source's center wavelength. Furthermore, the source bandwidth is given by $2/T_0$ and distinct-frequency plane-wave components within this bandwidth are uncorrelated. In words, phase-insensitive coherence is both *monochromatic* and *quasimonoplanatic*. The former feature is evident from the delta-function temporal-frequency term in Eq. (3). To better understand the latter, consider the plane-wave components at a given detuning, Ω. They only have significant excitation within the source's radiation cone, which has full cone angle $2\lambda_0/\pi\rho_0$. More importantly, these plane-wave components are only correlated with

*A phase-insensitive or phase-sensitive correlation function is stationary if it depends solely on the time difference t_2-t_1. Otherwise it is nonstationary.

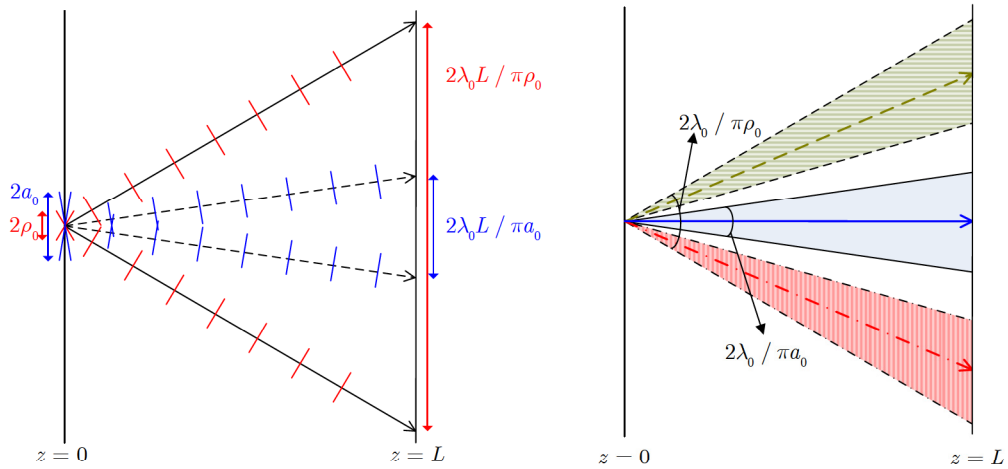

(a) Far-field coherence. (b) Angular spectrum.

Figure 1. The coherence behavior and the angular spectrum of the source-plane ($z=0$) baseband field operator $\hat{E}(\boldsymbol{\rho},t)$ with *phase-insensitive* correlation function given by Eq. (1). (a) The average $z=L$ plane irradiance is only appreciable within a region of diameter $2\lambda_0 L/\pi\rho_0$ (red) around the optical axis. The phase-insensitive fluctuations seen at two transverse points that are symmetrically displaced from the optical axis are correlated only when their separation is less than $2\lambda_0 L/\pi a_0$ (blue). (b) Three plane-wave components are shown as arrows with different colors (and line styles). The plane waves (of the same frequency) with which they have phase-insensitive correlation lie within the shaded cones of the same color (and same line-style borders). Because phase-insensitive coherence is quasimonoplanatic, the coherence cone for each plane wave is centered on its own propagation direction.

neighboring frequency-Ω plane-wave components that lie within the source's coherence cone, whose cone angle, $2\lambda_0/\pi a_0$, is much smaller than that of the radiation cone. This spatial-coherence behavior of the phase-insensitive correlation is illustrated in Fig. 1(b).

The phase-insensitive coherence behavior that we have just reviewed is well known,[2,3] but it will help us develop an analogous interpretation for phase-sensitive coherence behavior, which has received much less attention. Suppose that the phase-sensitive correlation function is given by the same Gaussian-Schell model,

$$\langle \hat{E}(\boldsymbol{\rho}_1,t_1)\hat{E}(\boldsymbol{\rho}_2,t_2)\rangle = \frac{2P_s}{\pi a_0^2} e^{-(|\boldsymbol{\rho}_1|^2+|\boldsymbol{\rho}_2|^2)/a_0^2 - |\boldsymbol{\rho}_2-\boldsymbol{\rho}_1|^2/2\rho_0^2} e^{-(t_2-t_1)^2/2T_0^2}, \tag{4}$$

where $P_s \equiv \int_{\mathbb{R}^2} \mathrm{d}\boldsymbol{\rho}\,\langle \hat{E}^2(\boldsymbol{\rho},t)\rangle$ is the mean-squared phase-sensitive flux, and a_0, $\rho_0 \ll a_0$, and T_0 are now, respectively, the radius of mean squared phase sensitive excitation, the coherence length, and the coherence time of that excitation. Consequently, $\hat{E}(\boldsymbol{\rho}_1,t_1)$ and $\hat{E}(\boldsymbol{\rho}_2,t_2)$ have appreciable phase-sensitive correlation when $\boldsymbol{\rho}_1$ and $\boldsymbol{\rho}_2$ are both within the phase-sensitive excitation radius a_0, have spatial separation less than the coherence length ρ_0, and temporal separation less than the coherence time T_0. Except for this source-plane description involving phase-sensitive correlation, rather than phase-insensitive correlation, it is unchanged from what we saw in conjunction with Eq. (1). The angular spectrum associated with the phase-sensitive correlation, however, reveals a rather different and quite interesting picture, as we will now show.

Applying the inverse transform associated with Eq. (2) to Eq. (4) we obtain

$$\langle \hat{A}(\boldsymbol{k}_1,\Omega_1)\hat{A}(\boldsymbol{k}_2,\Omega_2)\rangle = \frac{P_s T_0 \rho_0^2}{\sqrt{2\pi}} e^{-a_0^2|\boldsymbol{k}_s|^2/2} e^{-\rho_0^2|\boldsymbol{k}_d|^2/8} e^{-T_0^2\Omega_2^2/2}\delta(\Omega_2+\Omega_1), \tag{5}$$

where $\boldsymbol{k}_s \equiv (\boldsymbol{k}_1+\boldsymbol{k}_2)/2$ and $\boldsymbol{k}_d \equiv \boldsymbol{k}_2-\boldsymbol{k}_1$ as before, and we have again used the low-coherence $1/a_0^2+1/\rho_0^2 \approx 1/\rho_0^2$ approximation. Thus, as illustrated in Fig. 2(a), the angular extent of phase-sensitive excitation (found by setting $\boldsymbol{k}_d=\boldsymbol{0}$) is $2\lambda_0/\pi a_0$, and the angular extent of the phase-sensitive correlation (found by setting $\boldsymbol{k}_s=\boldsymbol{0}$), is given by $2\lambda_0/\pi\rho_0$. The source bandwidth is $2/T_0$ and plane-wave pairs with antipodal detunings within this bandwidth have nonzero phase-sensitive cross correlation, but all other frequency pairs are uncorrelated. It follows that

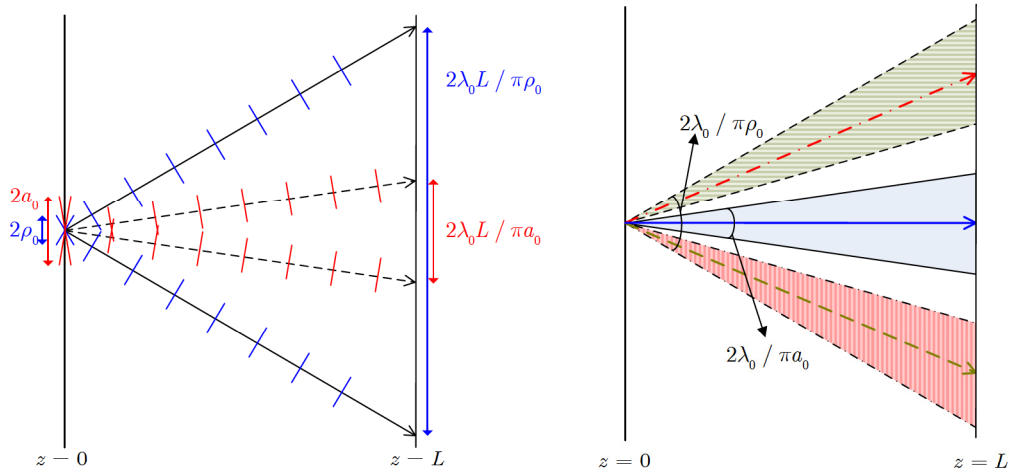

(a) Far-field coherence. (b) Angular spectrum.

Figure 2. The coherence behavior and the angular spectrum of the source-plane ($z = 0$) baseband field operator $\hat{E}(\boldsymbol{\rho}, t)$ with the *phase-sensitive* correlation function given in Eq. (4). (a) The mean-square phase-sensitive fluctuations on the $z = L$ plane are appreciable within the diameter $2\lambda_0 L/\pi a_0$ (red). The phase-sensitive fluctuations seen at two transverse points displaced in the opposite direction by an equal amount are correlated as long as the distance between the two points is less than $2\lambda_0 L/\pi\rho_0$ (blue). (b) Three plane-wave components are shown as three arrows with different colors (and line styles). The plane waves with which they have phase-sensitive correlation are shown as shaded cones having the same color (and same line-style borders). Because phase-sensitive coherence is quasibiplanatic, the coherence cone for each plane-wave component is centered around its mirror image about the optical axis.

phase-sensitive light is *bichromatic* and *quasibiplanatic*. The former feature is due to the delta-function temporal-frequency term in Eq. (5). To better appreciate the latter, consider the plane-wave components at $\pm(\boldsymbol{k}, \Omega)$. Each has appreciable phase-sensitive flux only when $\theta \equiv \lambda_0|\boldsymbol{k}|/2\pi$ lies within the source phase-sensitive radiation cone, which has full cone angle $2\lambda_0/\pi\rho_0$. More importantly, the $(\boldsymbol{k}, \Omega)$ plane-wave component only has phase-sensitive cross correlation with the frequency $-\Omega$ plane-wave components whose spatial frequencies lie within its coherence cone, which is centered at $-\theta$ in angle ($-\boldsymbol{k}$ in spatial frequency) and has cone angle $2\lambda_0/\pi a_0$. This spatial coherence structure of phase-sensitive correlation is illustrated in Fig. 2(b). Thus, although we have started with identical correlation functions for the two coherence classes, we have found that the physics implied by the two classes of coherence is notably different.

Bichromatic and biplanatic light-wave behavior is observed in signal and idler beams generated by continuous-wave (cw), frequency-degenerate spontaneous parametric downconversion (SPDC), which is the predominant nonclassical source for ghost-imaging experiments. SPDC with an $\mathbf{i}_z$-propagating, plane-wave, cw pump is a photon-fission process in which a single pump photon at frequency ω_P and with wave-vector $k_p\mathbf{i}_z$ (where $\mathbf{i}_z \cdot \mathbf{i}_z = 1$) splits into a signal-idler pair whose frequencies, ω_S and ω_I, obey $\omega_S + \omega_I = \omega_P$ due to energy conservation, and whose wave vectors, $\boldsymbol{k}_S$ and $\boldsymbol{k}_I$, satisfy $\boldsymbol{k}_S + \boldsymbol{k}_I = k_P\mathbf{i}_z$ as a result of momentum conservation. Consequently, the signal and idler photon pairs have bichromatic frequencies about $\omega_P/2$ and their transverse wave vectors are antipodal, resulting in biplanatic propagation. This is why the perturbative derivation of the output state of SPDC results in a biphoton wave function with the same propagation characteristics as the phase-sensitive correlation function.[11] A field-operator derivation of the signal and idler outputs from frequency-degenerate SPDC is obtained by quantizing the coupled-mode equations for the signal and idler as they propagate through the $\chi^{(2)}$ nonlinear crystal pumped with a nondepleting cw plane-wave pump.[12,13] This yields a Bogoliubov-type transformation of the signal and idler field operators at the input facet of the crystal to those at the output facet.[10] When the signal and idler inputs are in their vacuum states, the output field operators are in a zero-mean Gaussian state, with equal phase-insensitive autocorrelation functions, zero phase-insensitive cross correlation, and a nonzero phase-sensitive cross correlation that is stronger than what is attainable with any classical two-field Gaussian state having the same phase-insensitive autocorrelation functions.[14] When the Gaussian-Schell model in Eq. (1) is assumed for the phase-insensitive autocorrelation functions $\langle \hat{E}_S^\dagger(\boldsymbol{\rho}_1, t_1)\hat{E}_S(\boldsymbol{\rho}_2, t_2)\rangle$ and $\langle \hat{E}_I^\dagger(\boldsymbol{\rho}_1, t_1)\hat{E}_I(\boldsymbol{\rho}_2, t_2)\rangle$,

this stronger-than-classical phase-sensitive cross correlation is equal to[10]

$$\langle \hat{E}_S(\boldsymbol{\rho}_1, t_1)\hat{E}_I(\boldsymbol{\rho}_2, t_2)\rangle = \frac{2P}{\pi a_0^2} e^{-(|\boldsymbol{\rho}_1|^2+|\boldsymbol{\rho}_2|^2)/a_0^2}\left[i\, e^{-|\boldsymbol{\rho}_2-\boldsymbol{\rho}_1|^2/2\rho_0^2} e^{-(t_2-t_1)^2/2T_0^2} + (2/\pi)^{1/4}\sqrt{\frac{a_0^2}{PT_0\rho_0^2}}\, e^{-|\boldsymbol{\rho}_2-\boldsymbol{\rho}_1|^2/\rho_0^2} e^{-(t_2-t_1)^2/T_0^2}\right]. \quad (6)$$

When the source brightness is high, i.e., $\mathcal{I} \equiv PT_0\rho_0^2/a_0^2 \gg 1$, the first term in the square brackets dominates the latter term, and the maximum quantum-mechanically permissible phase-sensitive cross-correlation magnitude approaches the limit set by classical physics. However, when $\mathcal{I} \ll 1$, the second term is much larger than the first, resulting in a much stronger phase-sensitive cross correlation than permitted in a classical state. If the flux is then low enough that there is on average much less than one photon-pair emitted during a measurement interval, then the state of these SPDC outputs is well approximated by a dominant vacuum component plus a weak pair of entangled photons, viz., the biphoton state.[12,14] Therefore, as we shall show shortly, those characteristics of SPDC ghost imaging that are a consequence of the phase-sensitive nature of the cross correlation between the two beams are precisely those that can be mimicked by classical-state phase-sensitive light, whereas, the characteristics that stem from the stronger-than-classical nature of this cross correlation are intrinsically quantum effects.[10]

We conclude our treatment of coherence theory by describing the far-field, quasimonochromatic, paraxial propagation of the phase-insensitive and phase-sensitive correlation functions. The far-field, phase-insensitive correlation function is readily obtained from the source's phase-insensitive angular spectrum with the simple substitution of $2\pi\boldsymbol{\rho}/\lambda_0 L$ for $\boldsymbol{k}$. We find that the far-field phase-insensitive correlation function, stemming from the Gaussian-Schell near-field correlation function of Eq. (1), results in the far-field intensity radius being $a_L = \lambda_0 L/\pi\rho_0$ and the coherence radius being $\rho_L = \lambda_0 L/\pi a_0$. This behavior is well known from the Van Cittert-Zernike theorem for far-field phase-insensitive coherence propagation.[3] Phase-sensitive coherence propagates in a distinctly different manner. In this case we find that $\lambda_0 L/\pi a_0$ is the far-field mean-square radius and $\lambda_0 L/\pi\rho_0$ is the far-field coherence radius for the phase-sensitive correlation. Unlike the far-field phase-insensitive case, whose correlation peaks for two points with equal transverse-plane coordinates, the far-field phase-sensitive correlation is highest for two points that are symmetrically disposed about the origin on the transverse plane,[9–11] as expected from the quasibiplanatic nature of the phase-sensitive correlation.

3. STANDOFF GHOST IMAGING

Ghost imaging is a transverse imaging modality that has been receiving significant attention of late, owing to its novel physics and its potential use in remote sensing. Because the success of standoff ghost imaging hinges on reproducing the target's image from the diffusely back-scattered illumination that is sensed by the bucket detector, we will concentrate on the reflective ghost-imaging geometry shown in Fig. 3, in which the propagation distance L is well into the far field with respect to the source's coherence statistics.[3,9] Here, an image is formed by empirically evaluating the cross correlation between the photocurrents generated by the two spatially-separated photodetectors, which are illuminated by two highly-correlated, partially-coherent, and quasimonochromatic optical beams, both having center frequency ω_0. The signal (S) beam, whose baseband envelope we denote as $\hat{E}_S(\boldsymbol{\rho}, t)$, propagates L m from the source to the target through clear-air atmospheric turbulence, diffusely scatters from the surface, then propagates L m back before impinging on the single-pixel (i.e., bucket) photodetector. On the other hand, the reference (R) beam, whose baseband field operator is $\hat{E}_R(\boldsymbol{\rho}, t)$, propagates through L m of atmospheric turbulence in a different direction than the signal beam and illuminates the multi-pixel reference detector. The photocurrents from these photodetectors are cross correlated—by time averaging their product over a measurement interval spanning many source-field coherence times—to determine the target's average irradiance-reflection profile. Fundamentally, the physics that enables the formation of this image is the correlation between the far-field speckle patterns cast by the signal and reference beams. The reference arm's speckle pattern is resolved by the multi-pixel camera, and each measured speckle is utilized—via the cross-correlation operation—to estimate the fraction of the energy that has scattered back from the corresponding speckle that illuminated the target.

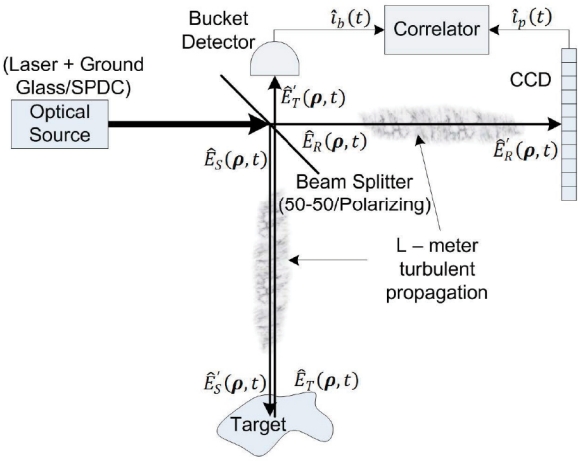

Figure 3. Configuration for lensless ghost imaging with quantum and classical sources. In both cases the optical source emits spatially-incoherent light that is separated into signal and reference beams by a beam splitter. For the quantum case, the source is a type-II phase-matched, frequency-degenerate, continuous-wave, parametric downconverter, and a polarizing beam splitter is used. For the classical case, the source is pseudothermal, i.e., laser light passed through a rotating ground-glass diffuser, and the beam splitter is 50-50 and nonpolarizing. The reference field travels L m to the CCD camera, while the signal field travels L m to the target, and the reflected light travels L m to the bucket detector. The image is then constructed in a continuous-time correlator.

In this section we consider two sources—one quantum and one classical—that have been previously utilized in ghost imaging experiments. For the quantum case, we investigate the image obtained using an SPDC source, whose orthogonally-polarized signal and idler output fields are split into the two arms of the ghost imager via a polarizing beam splitter. As we have shown in the previous section, this results in signal and reference fields that are in a zero-mean Gaussian state with the maximum phase-sensitive cross correlation permitted by quantum mechanics. In the low-brightness, low-flux operating regime, the SPDC source's output over a measurement interval can be taken to be a predominant vacuum component plus a biphoton. At high brightness, however, the SPDC source has a phase-sensitive cross correlation that approaches the limit set by classical physics. For the classical case, we consider a pseudothermal source realized by passing a cw laser beam through a rotating ground-glass diffuser, to render it spatially incoherent, followed by a 50-50 beam splitter to produce signal and reference fields with the maximum phase-insensitive cross correlation permitted by classical (and quantum) physics at any source brightness.

3.1 Propagation and Image Formation

There are three length-L optical propagation paths in Fig. 3: the reference path (R) from the source to the reference detector, the signal path (S) from the source to the target, and the target-return path (T) from the target to the bucket detector. We assume that clear-air atmospheric turbulence is present along all three paths, that they are statistically independent,[†] and that the paths are near-horizontal such that the refractive-index structure constant profiles, $C^2_{n,m}$ for $m \in \{R, S, T\}$, are constant.

We model the propagation along path $m \in \{R, S, T\}$ with the extended Huygens-Fresnel principle

$$\hat{E}'_m(\boldsymbol{\rho}', t) = \int d\boldsymbol{\rho}\, \hat{E}_m(\boldsymbol{\rho}, t) e^{\psi_m(\boldsymbol{\rho}', \boldsymbol{\rho})} \frac{k_0 e^{ik_0(L + |\boldsymbol{\rho}' - \boldsymbol{\rho}|^2/2L)}}{i2\pi L}, \tag{7}$$

where $k_0 \equiv \omega_0/c$, and we have suppressed the time delays.[‡] The turbulence-induced log-amplitude and phase

[†]The signal and the reference beams propagate through independent turbulence if their angular separation is greater than the isoplanatic angle.[15] The turbulence along the signal and target-return paths will be statistically independent if the one-way propagation duration exceeds the turbulence coherence time, or if the source and detector have angular separation relative to the target that exceeds the isoplanatic angle.

[‡]That no additional noise operator is needed to ensure that proper field commutators are preserved follows from the normal-mode decomposition of propagation through turbulence.[16]

fluctuations that are incurred along path m, from $\boldsymbol{\rho}$ to $\boldsymbol{\rho}'$, are encapsulated in the complex-valued $\psi_m(\boldsymbol{\rho}', \boldsymbol{\rho})$. For Kolmogorov-spectrum turbulence the correlation function of $e^{\psi_m(\boldsymbol{\rho}',\boldsymbol{\rho})}$ is

$$\langle e^{\psi_m^*(\boldsymbol{\rho}_1',\boldsymbol{\rho}_1)} e^{\psi_m(\boldsymbol{\rho}_2',\boldsymbol{\rho}_2)} \rangle = \exp\left(-1.45 k_0^2 C_{n,m}^2 L \int_0^1 ds\, |(\boldsymbol{\rho}_1' - \boldsymbol{\rho}_2')s + (\boldsymbol{\rho}_1 - \boldsymbol{\rho}_2)(1-s)|^{5/3} \right), \tag{8}$$

which does not lend itself to closed-form evaluation of the spatial resolution. Thus we will use the square-law approximation for this correlation function,[15]

$$\langle e^{\psi_m^*(\boldsymbol{\rho}_1',\boldsymbol{\rho}_1)} e^{\psi_m(\boldsymbol{\rho}_2',\boldsymbol{\rho}_2)} \rangle = e^{-(|\boldsymbol{\rho}_1'-\boldsymbol{\rho}_2'|^2 + (\boldsymbol{\rho}_1'-\boldsymbol{\rho}_2')\cdot(\boldsymbol{\rho}_1-\boldsymbol{\rho}_2) + |\boldsymbol{\rho}_1-\boldsymbol{\rho}_2|^2)/2\rho_m^2}, \tag{9}$$

where $\rho_m = (1.09 k_0^2 C_{n,m}^2 L)^{-3/5}$ is the transverse coherence length of the turbulence on path m.[§] Finally, because we are interested in standoff sensing, we will only consider targets in the far field of the source, i.e., we will assume $k_0 a_0 \rho_0 / 2L \ll 1$ for the (phase-insensitive) pseudothermal source, and $k_0 a_0^2 / 2L \ll 1$ for the (phase-sensitive) SPDC source.[9,10]

Targets of interest in standoff sensing often have surfaces that are very rough on the order of a wavelength, which diffusely reflect the incoming light into the hemisphere. Such objects are often quasi-Lambertian scatterers, i.e., they can be represented as an average amplitude reflection coefficient $\sqrt{\mathcal{T}(\boldsymbol{\rho})}$, where $\boldsymbol{\rho}$ is the transverse spatial coordinate on the target surface, times a spatially-varying random phase term that is due to height variations on the surface. Because this random phase is uncorrelated for transverse distances much greater than the wavelength of the illumination, the field reflection coefficient is modeled as a zero-mean complex Gaussian random process with a phase-insensitive autocorrelation

$$\langle T^*(\boldsymbol{\rho}_1) T(\boldsymbol{\rho}_2) \rangle = \lambda_0^2 \mathcal{T}(\boldsymbol{\rho}_1) \delta(\boldsymbol{\rho}_1 - \boldsymbol{\rho}_2) \tag{10}$$

insofar as propagation of the reflected light to the bucket detector is concerned. It is important to note that the target might absorb or transmit a portion of the light that illuminates it. The reflected field has thus suffered loss, and vacuum-state quantum noise must be injected to preserve the commutator relations, i.e., the field operator for the reflected light obeys $\hat{E}_T(\boldsymbol{\rho}, t) = \hat{E}_S'(\boldsymbol{\rho}, t)\sqrt{T(\boldsymbol{\rho})} + \hat{E}_{vac,S}(\boldsymbol{\rho}, t)\sqrt{1 - |T(\boldsymbol{\rho})|^2}$, where the field operator $\hat{E}_{vac,S}(\boldsymbol{\rho}, t)$ is in its vacuum state. This formalization requires that $|T(\boldsymbol{\rho})| \leq 1$ for all $\boldsymbol{\rho}$, which violates our previous assumption of a complex Gaussian distribution. In standoff sensing, however, the very small angular subtense of the bucket detector, relative to the 2π-SR hemisphere, implies that the average target-return flux collected by that detector will be so small a fraction of the flux illuminating the target that we can safely ignore this issue.[¶]

The photodetectors in both arms are assumed to have quantum efficiency $\eta < 1$ and finite bandwidth determined by a common impulse response $h_B(t)$, which is narrowband with respect to the field coherence time T_0.[10,17] The bucket detector produces the photocurrent $\hat{i}_b(t)$, while the reference detector's pixel centered at $\boldsymbol{\rho}_1$ produces a photocurrent $\hat{i}_p(t)$. The image is constructed as a pixelwise time-average cross correlation, so that the image at $\boldsymbol{\rho}_1$ is obtained from

$$\hat{C}(\boldsymbol{\rho}_1) \equiv \frac{1}{T_I} \int_{-T_I/2}^{T_I/2} dt\, \hat{i}_p(t) \hat{i}_b(t), \tag{11}$$

where T_I is the correlator's integration time.

3.2 Spatial Resolution and Image Contrast

To derive the spatial resolution and image contrast of ghost images obtained in reflection, we look at the ensemble average of the cross-correlation function $\langle \hat{C}(\boldsymbol{\rho}_1) \rangle$. We start by writing the cross correlation in terms of

[§]It is worth noting that this result does *not* assume that ψ_m is Gaussian distributed, and hence is neither restricted to the weak-perturbation propagation regime for turbulence, nor does it imply that the turbulence-induced fluctuations are purely phase tilt.

[¶]For a 10-cm-diameter bucket detector and a 10 km standoff range, the target-return flux is $\sim 10^{-10}\times$ the flux diffusely reflected from the target.

the photon flux impinging on the detectors, and then use Eq. (7) and the target-interaction beam-splitter relation to propagate the field at the bucket detector surface, $\hat{E}'_T(\boldsymbol{\rho}, t)$, back to the propagated signal field $\hat{E}'_S(\boldsymbol{\rho}, t)$. We then back-propagate along the signal and reference arms to the source, again with Eq. (7). Recognizing the independence of the source-, turbulence- and target-induced fluctuations, the mean image can be written as an integral expression involving the product of a fourth-order moment of the source fields, three second-order moments of the turbulence, and a second-order moment of the target's field-reflection coefficient. The turbulence and target moments are evaluated with Eqs. (9) and (10), and the fourth-order field moment is decomposed, via the moment-factoring theorem for Gaussian states,[2] as

$$\begin{aligned}\langle \hat{E}_R^\dagger(\boldsymbol{\rho}'_1, \tau_1)\hat{E}_S^\dagger(\boldsymbol{\rho}'_2, \tau_2)\hat{E}_R(\boldsymbol{\rho}''_1, \tau_1)\hat{E}_S(\boldsymbol{\rho}''_2, \tau_2)\rangle &= \langle \hat{E}_R^\dagger(\boldsymbol{\rho}'_1, \tau_1)\hat{E}_S^\dagger(\boldsymbol{\rho}'_2, \tau_2)\rangle\langle \hat{E}_R(\boldsymbol{\rho}''_1, \tau_1)\hat{E}_S(\boldsymbol{\rho}''_2, \tau_2)\rangle \\ &+ \langle \hat{E}_R^\dagger(\boldsymbol{\rho}'_1, \tau_1)\hat{E}_R(\boldsymbol{\rho}''_1, \tau_1)\rangle\langle \hat{E}_S^\dagger(\boldsymbol{\rho}'_2, \tau_2)\hat{E}_S(\boldsymbol{\rho}''_2, \tau_2)\rangle + \langle \hat{E}_R^\dagger(\boldsymbol{\rho}'_1, \tau_1)\hat{E}_S(\boldsymbol{\rho}''_2, \tau_2)\rangle\langle \hat{E}_S^\dagger(\boldsymbol{\rho}'_2, \tau_2)\hat{E}_R(\boldsymbol{\rho}''_1, \tau_1)\rangle. \quad (12)\end{aligned}$$

This expansion of the fourth-order moment for Gaussian states identifies the crux of the coherence behavior that yields a ghost image. For general Gaussian-state sources, both the phase-sensitive cross correlation and the phase-insensitive cross correlation contribute to the image signature, and the phase-insensitive autocorrelation term yields a featureless background.[10] For a pseudothermal source, the phase-sensitive cross correlation is zero, thus ghost-image formation is governed by the phase-insensitive cross correlation alone. For an SPDC source, however, the phase-insensitive cross-correlation vanishes and the ghost image is due to the phase-sensitive cross correlation between the two beams.

Using the Gaussian-Schell model correlation function from Eq. (1) for the pseudothermal source and the square-law approximation for the turbulence moments, we find that the ensemble-average image is given by

$$\langle \hat{C}(\boldsymbol{\rho}_1)\rangle_C = \frac{q^2\eta^2 A_p A_b}{L^2}\left(\frac{2P}{\pi a_L^2}\right)^2 \int d\boldsymbol{\rho}_2\, \mathcal{T}(\boldsymbol{\rho}_2)\left[1 + \frac{e^{-|\boldsymbol{\rho}_2-\boldsymbol{\rho}_1|^2/\alpha\rho_L^2}}{\alpha}\right], \quad (13)$$

where ρ_L and a_L, defined in the previous section, are the transverse coherence length and the beam radius after L m vacuum propagation, respectively. On the other hand, using the phase-sensitive cross correlation in Eq. (6) for the SPDC source, we find

$$\langle \hat{C}(\boldsymbol{\rho}_1)\rangle_Q = \left(\frac{2P}{\pi a_L^2}\right)\frac{A_p A_b q^2\eta^2}{L^2}\int d\boldsymbol{\rho}_2 \mathcal{T}(\boldsymbol{\rho}_2)\left[1 + \frac{e^{-|\boldsymbol{\rho}_2+\boldsymbol{\rho}_1|^2/\alpha\rho_L^2}}{\alpha}\left(1 + \frac{1}{\sqrt{8\pi\mathcal{I}}}\right)\right], \quad (14)$$

as the image signature. Here we have used the subscript C to refer to the classical-state results, and Q to refer to quantum-state results. The parameter α, which quantifies the turbulence-induced loss of spatial resolution, satisfies

$$\alpha = \frac{2\rho_R^2\rho_S^2 + a_0^2(\rho_R^2 + \rho_S^2)}{2\rho_R^2\rho_S^2} \geq 1, \quad (15)$$

and $\mathcal{I} = P\mathcal{I}_0\rho_0^2/a_0^2$ is again the source brightness in photons per spatiotemporal mode.

Both the classical and quantum ensemble-average cross correlations are sums of the same featureless background term plus an image-bearing term that is $\mathcal{T}(\boldsymbol{\rho})$ blurred by a Gaussian point-spread function of e^{-1} width $\rho_L\sqrt{\alpha}$. Thus, regardless of which correlation—phase insensitive or phase sensitive—is responsible for the image term, the far-field spatial resolution is identical. The SPDC image term differs from the pseudothermal's only by inversion of the image coordinates, and by the scaling $1 + 1/\sqrt{8\pi\mathcal{I}}$. The coordinate inversion results from the phase-sensitive nature of the correlation, while the scaling is a signature of the stronger-than-classical correlation.

We define the image contrast to be the difference between the brightest and darkest pixels in the image, normalized by the featureless background level.[14] Assuming that the target's features are fully resolved in the image, so that we can approximate the point-spread functions in Eqs. (13) and (14) as delta functions with respect to $\mathcal{T}(\boldsymbol{\rho})$, we arrive at

$$\mathcal{C}_C = \frac{\pi\rho_L^2}{A_T} \quad (16)$$

$$\mathcal{C}_Q = \frac{\pi\rho_L^2}{A_T}\left(\frac{1}{\sqrt{8\pi\mathcal{I}}} + 1\right), \quad (17)$$

where $A_T \equiv \int d\boldsymbol{\rho}\, \mathcal{T}(\boldsymbol{\rho})$ is the target's average cross-section for reflection. In the high-brightness, $\mathcal{I} \gg 1$, regime we see that $\mathcal{C}_Q$ converges to $\mathcal{C}_C$, as expected. In the low-brightness regime, however, the SPDC ghost image exhibits very nonclassical high-image-contrast behavior, which is due to its being formed from a stream of biphotons. We should note, in this regard, that our contrast evaluation has presumed DC-coupled operation of our correlator. Were we to use an AC-coupled correlator, then both the pseudothermal and SPDC ghost images would have high contrast.

3.3 Signal-to-Noise Ratio

We define the signal-to-noise ratio (SNR) to be the ratio of the squared mean of the cross-correlation function to its variance, i.e.,

$$\mathrm{SNR} = \frac{\langle \hat{C}(\boldsymbol{\rho}_1)\rangle^2}{\mathrm{Var}[\hat{C}(\boldsymbol{\rho}_1)]} = \frac{\langle \hat{C}(\boldsymbol{\rho}_1)\rangle^2}{\langle \hat{C}^2(\boldsymbol{\rho}_1)\rangle - \langle \hat{C}(\boldsymbol{\rho}_1)\rangle^2}. \tag{18}$$

The primary complication in evaluating the SNR is in the second-order moment

$$\langle \hat{C}^2(\boldsymbol{\rho}_1)\rangle = \frac{1}{T_I^2}\int_{-T_I/2}^{T_I/2} dt \int_{-T_I/2}^{T_I/2} du\, \langle \hat{i}_p(t)\hat{i}_b(t)\hat{i}_p(u)\hat{i}_b(u)\rangle, \tag{19}$$

which, after back-propagating to the source, requires that we evaluate an eighth-order moment of the source fields, two sixth-order moments of the source fields, a fourth-order moment of the source fields, a fourth-order moment of the target, and three fourth-order moments of the turbulence.

We are mainly concerned with the SNR behavior obtained with pseudothermal and SPDC sources, as a result of their different coherence properties. Moreover, as there is no simple way to evaluate the fourth-order turbulence moments, we will evaluate the SNR for these two sources under the assumption of turbulence-free propagation. We also assume that the photodetectors are AC-coupled, and that the imager can fully resolve the target's spatial features. All remaining higher-order moments are written as the sum of the product of second-order moments through application of the Gaussian moment-factoring theorem. To simplify the final expressions we define two new terms, $A_T' \equiv \int d\boldsymbol{\rho}\, \mathcal{T}^2(\boldsymbol{\rho})$, and $\Gamma \equiv \int d\boldsymbol{\nu}\ e^{-|\boldsymbol{\nu}|^2/2} O(\boldsymbol{\nu}, 4\sqrt{\beta})/(4\pi\beta)^2$, where $O(\boldsymbol{\zeta}, D)$ is the two-circle overlap function for circles of diameter D,

$$O(\boldsymbol{\zeta}, D) = \begin{cases} (D^2/2)\left[\cos^{-1}\left(\frac{|\boldsymbol{\zeta}|}{D}\right) - \frac{|\boldsymbol{\zeta}|}{D}\sqrt{1-\frac{|\boldsymbol{\zeta}|^2}{D^2}}\right], & \text{for } |\boldsymbol{\zeta}| \le D \\ 0, & \text{else,} \end{cases} \tag{20}$$

with $\boldsymbol{\nu} = \rho_L k_0(\boldsymbol{\rho}' - \boldsymbol{\rho}'')/L$ for $\boldsymbol{\rho}'$ and $\boldsymbol{\rho}''$ being transverse coordinate vectors on the bucket detector's photosensitive surface. We also introduce $\beta \equiv A_b/\pi a_0^2$ as the ratio of the bucket detector's receiving area to the transmitter beam's area. We have that Γ is a monotonically decreasing function of increasing β, something that will be important in understanding the ghost image's speckle-limited saturation SNR.

Both A_T' and Γ have significant physical interpretations. A_T' is a measure of the target's reflection cross-section. As such it is directly related to the number of on-target resolution cells and, therefore, the time it takes to form an image. Γ is a measure of the spatial averaging of target-induced speckle that occurs at the bucket detector. Because the signal field causes speckles on the target that are, in the absence of turbulence, of an average extent ρ_L, we can regard the illumination field as a collection of uncorrelated patches of this size. The rough surface randomizes the reflected field produced by each illumination speckle, so that when propagated into the far field it will have an intensity radius that is much larger than the bucket detector's area, A_b, with a coherence radius of $\sim 2L/k_0\rho_L \approx a_0$. The amount of aperture averaging of the returns from different illumination speckles, encapsulated in Γ, is then purely a function of β.

Even under the preceding assumptions, the ghost-image SNR is given by a complicated expression that involves noise from three different sources—the randomness of the source, the randomness from scattering from the rough surface, and detection noise—as well as their cross terms.[18] Here we highlight three limiting cases. First,

we consider ghost images formed with very long integration times, so $T_I/T_0 \gg 1$. For both the pseudothermal and the SPDC sources the ghost-image SNR approaches a maximum value, the saturation SNR, given by

$$\lim_{T_I/T_0\to\infty} \mathrm{SNR} = \mathrm{SNR}_{\mathrm{sat}} \equiv 1/\Gamma. \tag{21}$$

$\mathrm{SNR}_{\mathrm{sat}}$ corresponds to performance limited by the target-induced speckle: because the target is motionless so too is that speckle, and its randomness is not averaged out by a long integration time. The image fluctuations contributed by source randomness and detection noise, however, are reduced by the time integration, because they have finite coherence times. In order to increase $\mathrm{SNR}_{\mathrm{sat}}$, we must increase β, which demonstrates a fundamental trade-off between spatial resolution and SNR in that once A_b has been increased to its maximum feasible size, the only way to further increase β is to decrease a_0. However, the spatial resolution ρ_L is inversely proportional to a_0, so increasing $\mathrm{SNR}_{\mathrm{sat}}$ this way will degrade resolution.

Next, let us consider what happens with a high-brightness source ($\mathcal{I} \gg 1$) when the integration time is too short for the SNR to approach its target-speckle-limited maximum value. For both the pseudothermal and the SPDC sources we then have that

$$\mathrm{SNR} \approx \mathrm{SNR}_H \equiv \frac{T_I}{T_0}\frac{\sqrt{2\pi}\rho_L^2}{A_T'(1+1/\beta)}\mathcal{T}^2(\boldsymbol{\rho}_1). \tag{22}$$

This limit is dominated by the need to resolve different resolution cells on the target by way of correlation. Thus, it is directly proportional to the normalized integration time, T_I/T_0: we need to see many different realizations of the source fields to determine the reflection coefficient from the correlations. This term is also inversely proportional to the number of on-target resolution cells, A_T'/ρ_L^2; the more resolution cells there are, the longer it takes to deduce the spatial pattern of the target.

Finally, let us look at the low-brightness regime ($\mathcal{I} \ll 1$), once again keeping the detector integration time short enough to avoid target-speckle-limited performance. Here we find that

$$\mathrm{SNR} \approx \mathrm{SNR}_{L,C} \equiv \frac{16\sqrt{2}}{\sqrt{\pi}}\frac{T_I}{T_0}\frac{A_p\eta^2\mathcal{I}^2}{\Omega_B T_0\rho_L^2}\mathcal{T}(\boldsymbol{\rho}_1)\frac{A_b}{L^2} \tag{23}$$

for the pseudothermal source, and

$$\mathrm{SNR} \approx \mathrm{SNR}_{L,Q} \equiv \frac{8}{\pi}\frac{T_I}{T_0}\frac{A_p\eta^2\mathcal{I}}{\Omega_B T_0\rho_L^2}\mathcal{T}(\boldsymbol{\rho}_1)\frac{A_b}{L^2}, \tag{24}$$

for the SPDC source where, as before, the subscripts C and Q denote classical and quantum sources, respectively. Here, A_p and Ω_B are the reference detector's pixel area, and the bandwidth of the photodetector's impulse response $h_B(t)$. This SNR limit is dominated by detection noise, and, as such, it is significantly different for the classical and quantum sources, with the latter's performance being far superior to the former's. The scaling factor A_b/L^2 is the solid angle subtended by the bucket detector at the target, hence it is the fraction of the reflected light that detector collects. Note that classical phase-sensitive light, in the low-brightness regime, leads to the same SNR expression as given above for the phase-insensitive source.

In summary, coherence theory for phase-insensitive and phase-sensitive light reveals that ghost-image formation in reflection originates from the propagation of the cross correlation between the signal and reference fields. The reference measurement provides knowledge of the on-target irradiance pattern, which allows us to reconstruct that target's intensity-reflection profile. For far-field operation, the phase-insensitive source yields an erect ghost image whereas the phase-sensitive source produces an inverted ghost image. If the phase-sensitive source is a low-brightness downconverter, i.e., a quantum source, then its DC-coupled image contrast will greatly exceed the corresponding value obtained with a phase-insensitive source. Moreover, the quantum source's image SNR will greatly exceed that of its low-brightness phase-insensitive counterpart.

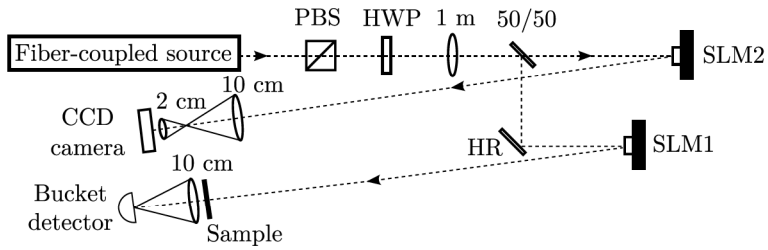

Figure 4. Experimental setup. PBS: polarizing beam splitter, HWP: half-wave plate, SLM: spatial light modulator, CCD: charge-coupled device (camera), HR: high-reflection mirror.

4. EXPERIMENTAL DEMONSTRATION OF GHOST IMAGING WITH A CLASSICAL PHASE-SENSITIVE SOURCE

Early ghost imaging experiments, such as that of Pittman *et al.*,[19] employed biphotons generated by SPDC and attributed image formation to quantum entanglement. As shown in Section 3, SPDC-based ghost imaging is a consequence of the phase-sensitive coherence between the source's signal and idler beams. Later experiments[20–22] demonstrated ghost imaging using classical pseudothermal light. As shown in Section 3, pseudothermal ghost imaging arises from the phase-insensitive coherence between the signal and reference beams exiting the 50-50 beam splitter in Fig. 3. The unified theory of ghost imaging for Gaussian-state illumination under the umbrella of (phase-insensitive and phase-sensitive) coherence theory suggests that classical light sources exhibiting phase-sensitive coherence should also yield ghost images, and furthermore, they should mimic the features of biphoton-state ghost imaging that are a consequence of the phase-sensitive correlation between the signal and idler photons.[10]

In this section we report on an experimental demonstration of ghost imaging with classical phase-sensitive light. Using a pair of synchronized spatial light modulators (SLMs), which impose programmable phases at individually addressable pixels, we have constructed a system to demonstrate far-field phase-sensitive ghost imaging using classical light and standard photodetectors.[23] Our experimental setup is shown in Fig. 4. A 10 mW, $\lambda_0 = 795$ nm cw laser beam was first split into signal and reference arms by a 50-50 beam splitter. Each beam was focused to a waist of $w_0 \approx 200\,\mu$m and modulated by a reflective SLM placed at the waist. The SLMs, manufactured by Boulder Nonlinear Systems, each had 512×512 individually addressable pixels with a pixel size of $7.68 \times 7.68\,\mu$m. Given the size of the beam waist, we chose to modulate only the center 128×128 pixels of each SLM, driving both arms with uniformly-distributed, computer-generated random phases. We estimate the phase accuracy of the SLMs to be ≈ 20 mrad for most phase values. We were able to program SLM1 and SLM2 shown in Fig. 4 to synchronously apply either identical or complementary random patterns, which corresponded to the imposition of phase-insensitive or phase-sensitive cross correlations, respectively.

We placed our sample transmission mask in the signal arm at a distance of $L = 80$ cm from SLM1, which places us in the far-field regimes of both phase-sensitive and phase-insensitive coherence propagation,[10] because $\pi w_0^2/(\lambda_0 L) \approx 0.2$. We collected signal-arm light using a lens to focus the light transmitted through the mask onto a single-pixel Thorlabs PDA55 silicon detector. The reference arm used a Basler Pilot series charge-coupled device (CCD) camera with 1600×1200 pixels and 12 bits per pixel of dynamic range. Because the physical size of the CCD was significantly smaller than the transmission mask we placed in the signal arm, we utilized a two-lens $5.7\times$ telescope to minify the speckle pattern in the reference arm, allowing us to ghost image the entire region of our transmission mask.

We imaged a portion of a 1951 USAF resolution test target—in both phase-insensitive and phase-sensitive modes of operation—with the covariances computed over 18640 realizations, as shown in Fig. 5. Consistent with theory for far-field ghost imaging, we found the phase-sensitive ghost image to be inverted, whereas the phase-insensitive ghost image was erect. We also observed similar spatial resolutions for both modes of operation, as predicted by their equal far-field coherence radii, $\rho_L = \lambda_0 L/(\pi w_0)$. The measured spatial resolution was roughly consistent with our observed $\sim$1 mm speckle radius. Note that a bright artifact at the center of the image, caused primarily by the sub-optimal 83% fill factor of our SLMs, prevented us from imaging effectively near that region.

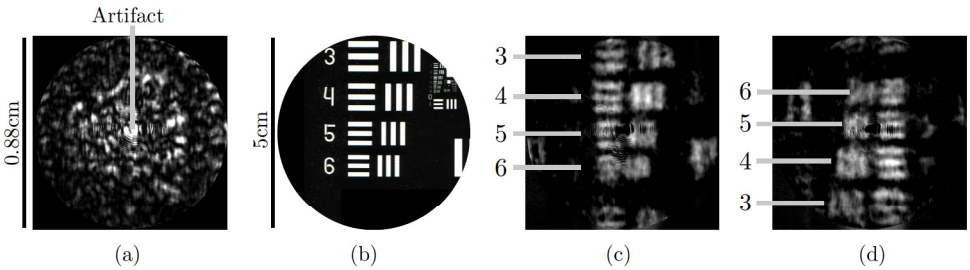

Figure 5. (a) Sample single-frame speckle pattern as imaged by the CCD. The artifact is due to the SLMs' ∼83% pixel fill factor. (b) Portion of a USAF spatial-resolution transmission mask used as the object. (c) Phase-insensitive and (d) phase-sensitive far-field ghost images, each averaged over 18640 realizations. Background noise levels are clipped for improved visibility.

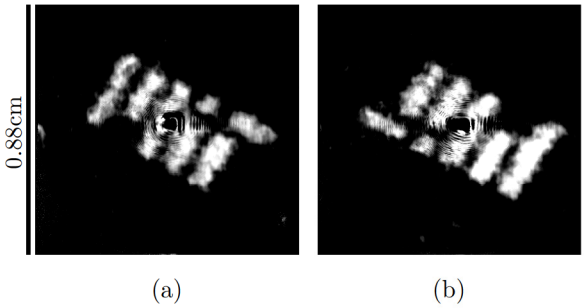

Figure 6. MIT-logo ghost images after 7000 realizations for (a) phase-insensitive and (b) phase-sensitive light, showing image inversion in the latter. The images are individually normalized, with the noise levels clipped for improved visibility. The bright-spot artifact at the center prevented us from obtaining an image in that small region.

Figure 6 shows a similar result of phase-sensitive and phase-insensitive ghost images of an MIT-logo transmission mask averaged over 7000 realizations, again confirming the inverted image obtained in the phase-sensitive case.

In performing phase-sensitive measurements, we noticed a curious effect in which the ghost images were badly degraded, for tightly-focused illumination, when the SLMs were not placed close enough to the beam waist. On the other hand, when the illumination was loosely-focused, we observed that the quality of the ghost images was far less sensitive to the axial displacement of the SLM from the beam waist. We demonstrate this effect in Fig. 7, which shows ghost images generated from a single-arm CCD-based setup that simulated the reference arm by alternating between signal and reference phase patterns as follows. In the odd-numbered frames, we applied the reference pattern to the SLM and recorded its CCD-camera far-field pattern—without any mask—as in standard ghost imaging. In even-numbered frames, we applied the corresponding (phase-sensitive or phase-insensitive) signal pattern to the SLM, recorded its CCD-camera far-field pattern, imposed a transmission mask on that pattern in software, and computed a simulated bucket-detector value by summing the resulting pixel values. By employing this single-SLM architecture we avoided discrepancies caused by the use of a two-SLM setup, which permitted us to study the focusing issue in isolation. Our results show that the quality of the phase-insensitive ghost image is not affected by the axial displacement of the SLM, whereas the phase-sensitive ghost image suffers a dramatic degradation when tight focusing is employed and there is axial displacement of the SLM from the beam waist. The displacement-induced degradation of phase-sensitive imaging that accompanies focus errors is explained by the phase-front present on a mislocated SLM under tight focusing. Suppose the same non-zero spherical phase-front is added to both the signal and reference at the SLMs. Phase-insensitive operation is unaffected by this addition, because it only requires the signal and reference arms to be perfectly correlated, i.e., to have equal phase-fronts. In contrast, phase-sensitive operation is degraded, because it requires the phases in the two arms to be perfectly anti-correlated, i.e., their phase-fronts should be complementary.

The signal-to-noise ratio (SNR) of a single pixel in a ghost image is defined as the ratio of the squared-mean value of that pixel, computed over multiple independent runs of the experiment, to the variance over those runs.

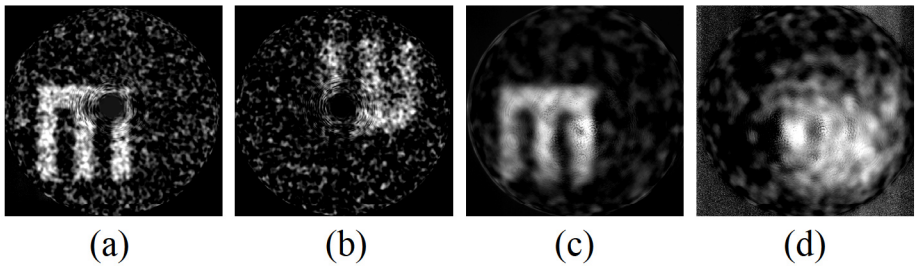

Figure 7. Comparison of far-field phase-sensitive ghost imaging under loose focusing ($w_0 = 150\,\mu$m) for (a) and (b), and tight focusing ($w_0 = 50\,\mu$m) for (c) and (d), with the SLM located at a distance of 2.75× the Rayleigh range z_R. The mask is an off-center letter M. Phase-insensitive images in (a) and (c) are not affected, but phase-sensitive measurements in (b) and (d) show degradation that is severe for tight focusing in (d).

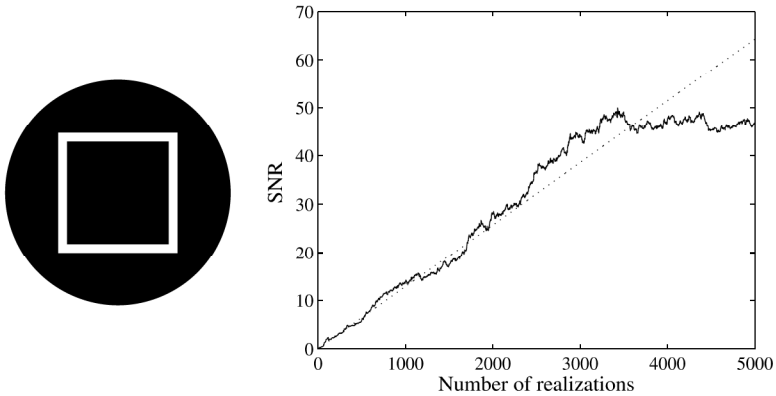

(a) (b)

Figure 8. (a) Mask used for signal-to-noise ratio (SNR) test. (b) SNR, approximated by spatial-averaging, in a simple beamsplitter-based phase-insensitive ghost imaging experiment of the mask shown in (a). The dotted curve shows the theoretical prediction. As the number of realizations increases beyond ∼3000, the experimental curve falls short of the theoretical prediction.

Because repeated running of our experiments would take a long time at the nominal speed of our equipment, we made an approximation by taking the spatial average over all transmitted parts of our image (noting that our mask was binary). For the 1951 USAF test target images, we obtain SNR values of ∼7.5 for the phase-insensitive measurement and ∼7.9 for the phase-sensitive measurement. The theoretical SNR for both cases is given by the narrowband high-brightness SNR asymptote, i.e., SNR= $\sqrt{2\pi}(T_I/T_0)(\rho_L^2/A_T)$, where A_T is the area of the mask, ρ_L is the coherence radius, and T_I/T_0 is the ratio of the integration time to the source coherence time. In our experiment $A_T = 3.5$ cm^2, and T_I/T_0 is equal to the number of realizations, 18640, yielding a theoretical SNR of 133.

While our experiment shows similar SNRs for both phase-sensitive and phase-insensitive modes of operation as expected, we are still well below the theoretically-achievable limit. We investigated this further in a ghost-imaging setup with a single SLM followed by a 50-50 beamsplitter and a phase-insensitive measurement, imaging a simple binary transmission mask consisting of the square outline shown in Fig. 8. Again, we spatially averaged over all transmitting parts of our image to approximate the true SNR. We observed that our empirically-calculated SNR agreed with the theoretical linear relationship between SNR and the number of realizations up to ∼3000 realizations, but then saturated. This saturation value, as well as the realization number at which it occurs, seemed to depend on the part of the image that was used in the spatially-averaged estimation of the SNR. Hence, the SNR saturation we have observed in experiment may be attributable to defects in the SLM or its phase calibration, or it may be an artifact of our approximation to the SNR via spatial-averaging, in the high SNR regime. We plan to continue investigating this issue in further detail.

In implementing our two-SLM system, we encountered several experimental challenges that are not present in SPDC or pseudothermal ghost imaging. First, and perhaps most obvious, is that the SLMs need to be well-

calibrated, well-synchronized, and precisely aligned with the beam location in order to impose maximal cross correlations: a misalignment or calibration error drastically affects the speckle pattern in the far-field, degrading the quality of the image. Second, for phase-sensitive imaging the SLMs need to be placed exactly at beam waist for optimal results; phase-insensitive imaging does not have this requirement. Third, low-cost SLMs may have a sub-unity pixel fill factor, resulting in artifacts in the speckle pattern (including the zeroth-order bright spot at the image's center) that affect our ability to image near such regions.

We plan to continue investigating variations of ghost imaging. Compressed sensing, which increases detection speed for objects having a sparse representation, has already been demonstrated by Katz *et al.*[24] Computational ghost imaging, proposed by Shapiro,[25] has been implemented by Bromberg *et al.*[26] To date we have performed our own preliminary tests of computational ghost imaging, and hope to improve our SNR through a better understanding of the caveats in simulating a far-field intensity pattern for our setup. We believe that exploration of computational ghost imaging may provide useful insights into adaptive imaging, in which the SLM modulation is driven with patterns constructed to maximize the information acquired about the object in each subsequent frame. We also plan to move our experiment to the 1550 nm wavelength, at which we may be able to construct a classical downconversion-based phase-sensitive source operating in the amplified high-flux SPDC regime.[27]

5. DISCUSSION

Despite the focus in traditional optical coherence theory on phase-insensitive coherence, a complete second-order characterization of optical fields requires that both phase-sensitive and phase-insensitive coherence properties be investigated. Furthermore, for Gaussian-state sources, phase-sensitive coherence theory is fundamental to unambiguously delineating the boundary between classical and quantum behavior. In this paper we have first reviewed the key propagation characteristics of phase-sensitive correlations and compared them to those of the well-known phase-insensitive correlations. Then, we have applied this theory to study ghost imaging for standoff sensing. We have reviewed the image formation process, spatial resolution, image contrast, and SNR attained with a pseudothermal (phase-insensitive) source, and an SPDC (phase-sensitive) source. We have quantified the impact of atmospheric turbulence on image resolution, and the impact of target-induced speckle on the SNR. Finally, we have reported a recent ghost imaging experiment using *classical* phase-sensitive light, which, to our knowledge, is the first demonstration of ghost imaging with such a source. Via this experiment we have validated the key predictions of our theory, e.g., that the image inversion seen in far-field phase-sensitive ghost imaging is a consequence of phase-sensitive coherence propagation physics, and not entanglement *per se*. We have also reviewed some experimental challenges with imaging using classical phase-sensitive light generated via SLMs.

Optical coherence theory has been of immense value to the design, analysis, and performance characterization of many classical optical engineering applications, including imaging, holography, lithography, spectroscopy, ranging, etc. The emergence of biphoton-state quantum imaging, in the past decade, has led to improvements in spatial resolution, image contrast, and in some cases SNR. However, a subset of these improvements have later been mimicked by classical light sources, raising a debate as to wherein lies the classical-quantum boundary. The lack of a common theoretical framework that can unify the treatment of these applications, when performed with either classical or quantum sources, has made it difficult to draw the boundary between classical and quantum behavior. With the extension of traditional optical coherence theory to include the study of phase-sensitive coherence, we are now able to bridge the gap between classical statistical optics and Gaussian-state quantum imaging.

In conclusion, we have presented the paraxial-propagation theory for phase-insensitive and phase-sensitive second-order correlation functions, applied it to the analysis of standoff ghost imaging, and have reported a recent ghost-imaging experiment with classical phase-sensitive light. The central theme to our paper has been the coherence theory for phase-sensitive light, and its utility in unifying classical and quantum Gaussian-state imaging.

ACKNOWLEDGMENTS

The contribution of BIE to this paper was supported by the DARPA InPho program under contract number PROP. 40-15391, and was carried out by the Jet Propulsion Laboratory, California Institute of Technology, under

a contract with the National Aeronautics and Space Administration. The contributions of NDH, DV, FNCW, and JHS to this paper were supported by the W. M. Keck Foundation Center for Extreme Quantum Information Theory and the DARPA InPho program through US Army Research Office Grant No. W911NF-10-1-0404.

REFERENCES

1. M. Born and E. Wolf, *Principles of Optics*, Cambridge Univ., Cambridge, 7th ed., 1999.
2. L. Mandel and E. Wolf, *Optical Coherence and Quantum Optics*, Cambridge Univ., Cambridge, 1995.
3. J. W. Goodman, *Statistical Optics*, Wiley, New York, Classics ed., 2000.
4. B. E. A. Saleh and M. C. Teich, *Fundamentals of Photonics*, Wiley, New Jersey, 2nd ed., 2007.
5. J. H. Shapiro, "Quantum Gaussian noise," in *Proc. SPIE*, **5111**, pp. 382–395, 2003.
6. H. P. Yuen and J. H. Shapiro, "Optical communication with two-photon coherent states—Part I: quantum state propagation and quantum noise reduction," *IEEE Trans. Inform. Theory* **24**, pp. 657–668, 1978.
7. Y. Shih, "Entangled photons," *IEEE J. Sel. Top. Quantum Electron.* **9**, pp. 1455–1467, 2003.
8. J. H. Shapiro and K.-X. Sun, "Semiclassical versus quantum behavior in fourth-order interference," *J. Opt. Soc. Am. B* **11**, pp. 1130–1141, 1994.
9. B. I. Erkmen and J. H. Shapiro, "Optical coherence theory for phase-sensitive light," in *Proc. SPIE*, **6305**, art. 63050G, 2006.
10. B. I. Erkmen and J. H. Shapiro, "Ghost imaging: from quantum to classical to computational," *Adv. Opt. Photon.* **2**, pp. 404–450, 2010.
11. B. E. A. Saleh, A. F. Abouraddy, A. V. Sergienko, and M. C. Teich, "Duality between partial coherence and partial entanglement," *Phys. Rev. A* **62**, art. 043816, 2000.
12. T. H. Kim, F. N. C. Wong, and J. H. Shapiro, "Efficient generation of polarization-entangled photons in a nonlinear crystal," *Laser Phys.* **16**, pp. 1517–1524, 2006.
13. E. Brambilla, A. Gatti, M. Bache, and L. A. Lugiato, "Simultaneous near-field and far-field spatial quantum correlations in the high-gain regime of parametric down-conversion," *Phys. Rev. A* **69**, art. 023802, 2004.
14. B. I. Erkmen and J. H. Shapiro, "Unified theory of ghost imaging with Gaussian-state light," *Phys. Rev. A* **77**, art. 043809, 2008.
15. L. C. Andrews and R. L. Phillips, *Laser Beam Propagation through Random Media*, SPIE, Bellingham, 2nd ed., 2005.
16. J. H. Shapiro, "Normal-mode approach to wave propagation in the turbulent atmosphere," *Appl. Opt.* **13**, pp. 2614–2619, 1974.
17. B. I. Erkmen and J. H. Shapiro, "Signal-to-noise ratio of Gaussian-state ghost imaging," *Phys. Rev. A* **79**, art. 023833, 2009.
18. N. D. Hardy, *Analyzing and Improving Image Quality in Reflective Ghost Imaging.* S.M. thesis, Massachusetts Institute of Technology, Cambridge, MA, 2011.
19. T. B. Pittman, Y. H. Shih, D. V. Strekalov, and A. V. Sergienko, "Optical imaging by means of two-photon quantum entanglement," *Phys. Rev. A* **52**, pp. R3429–R3432, 1995.
20. F. Ferri, D. Magatti, A. Gatti, M. Bache, E. Brambilla, and L. A. Lugiato, "High-resolution ghost image and ghost diffraction experiments with thermal light," *Phys. Rev. Lett.* **94**, art. 183602, 2005.
21. G. Scarcelli, V. Berardi, and Y. Shih, "Can two-photon correlation of chaotic light be considered as correlation of intensity fluctuations?," *Phys. Rev. Lett.* **96**, art. 063602, 2006.
22. R. Meyers, K. S. Deacon, and Y. Shih, "Ghost-imaging experiment by measuring reflected photons," *Phys. Rev. A* **77**, art. 041801(R), 2008.
23. D. Venkatraman, N. Hardy, F. N. C. Wong, and J. H. Shapiro, "Classical far-field phase-sensitive ghost imaging," *submitted to Opt. Lett.*, 2011.
24. O. Katz, Y. Bromberg, and Y. Silberberg, "Compressive ghost imaging," *Appl. Phys. Lett.* **95**, art. 131110, 2009.
25. J. H. Shapiro, "Computational ghost imaging," *Phys. Rev. A* **78**, art. 061802(R), 2008.
26. Y. Bromberg, O. Katz, and Y. Silberberg, "Ghost imaging with a single detector," *Phys. Rev. A* **79**, art. 053840, 2009.
27. J. Le Gouët, D. Venkatraman, F. N. C. Wong, and J. H. Shapiro, "Classical low-coherence interferometry based on broadband parametric fluorescence and amplification," *Opt. Express* **17**, pp. 17874–17887, 2009.